RESEARCH ARTICLE

A 0.15 μVrms Super-Sensitivity Photoacoustic Imager Based on Coherent Detection for Deep in-Vivo Imaging

CHUANSHI YANG, (Member, IEEE), **ZHONGYUAN FANG**, (Member, IEEE), **XIAOYAN TANG**, **ZESHENG ZHENG**, **KAI TANG**, AND **YUANJIN ZHENG**, (Senior Member, IEEE)

School of Electrical and Electronic Engineering, Nanyang Technological University, Singapore 639798

Corresponding author: Yuanjin Zheng (yjzheng@ntu.edu.sg)

ABSTRACT Among various multi-wave imaging methods, the photoacoustic imaging (PAI) has attracted more attention because it can achieve higher resolution and contrast through combining advantages of light excitation and ultrasound detection. However, due to low restricted laser fluence, large scattering and attenuation in tissue, and low energy conversion efficiency, high sensitivity is still imperative in the receiver to read out PA signals. A new photoacoustic receiver with mixed-signal coherent detection technique is developed and fabricated for the first time. Co-working with the early-late acquisition and tracking technique, the receiver can lock into the weak PA signal automatically. For the receiver system on chip (SoC), a high performance analog front-end (AFE) with a low noise amplifier (LNA), low-pass filter (LPF), programmable-gain amplifier (PGA), multiplier, successive-approximation analog-to-digital converter (SAR ADC) and digital-to-analog converter (DAC) are implemented on chip. Noise shaping (NS) technique is implemented in the SAR ADC to enhance the signal-to-noise ratio (SNR). Measurement results show that, the LNA achieves 0.23mPa$\sqrt{\text{(mW/Hz)}}$ noise efficiency factor (NEF) with the aid of resonant noise matching (RNM) technique, and the NS-SAR ADC can obtain 62.2dB signal-to-noise-and-distortion ratio (SNDR) in 10MHz bandwidth under 100MS/s sampling rate. The single channel receiver can achieve 135dB dynamic range and 0.15μVrms sensitivity. The output SNR can be improved by about 6dB after enabling the 4 channels. The power consumption of a single channel is 28.8mW. The contrast-to-noise ratio (CNR) of the images at 1cm depth is 44dB.

INDEX TERMS Photoacoustic imager, high sensitivity receiver, coherent detection, resonant noise matching, early-late acquisition and tracking, AFE, noise shaping SAR ADC.

I. NTRODUCTION

Photoacoustic imaging (PAI) is a rising technique that combines the advantages of both high optical contrast between different soft biological tissues and the high spatial resolution of pure ultrasound imaging. The imaging principle is illustrated in Fig. 1. The light excited from a laser diode is absorbed by the tissue and converted to heat. Then the absorbed energy causes transient thermoelastic expansion and wideband ultrasonic emission. Finally, the ultrasound

The associate editor coordinating the review of this manuscript and approving it for publication was Mauro Fadda.

signals are received by the ultrasound sensors and converted to electrical signals [1]. The laser will scan a specified area of the target one point by one point. The amplitude of each echo varies according to the tissues' absorbance of the laser and conversion efficiency to ultrasound energy. Thus, the amplitude can project to a pixel in the image. Consequently, an image can be constructed based on the amplitude of the echo and the coordinates of the laser scanning. Through such a method, the PA imaging can break through the optical scattering limitation in the pure optical imaging. The PA imaging modality has the advantages of non-invasive and rich contrast than other cross-sectional imaging modalities such

FIGURE 1. Principle and traditional system of photoacoustic imaging.

FIGURE 2. Working principle of the proposed coherent detection.

as computerized tomography (CT) and magnetic resonance imaging (MRI).

Even though the PA imaging has achieved tremendous progress, it is extremely challenging to realize deep tissue *in-vivo* imaging because of the following limitations: the fluence of laser is restricted to below 20mJ/cm^2 by the American national standards institute (ANSI) safety standard, the tissues can induce large attenuation and scattering, and the energy conversion efficiency from optical energy to acoustic is low. Consequently, the sensitivity of the imager becomes a significant challenge. To improve the sensitivity, many efforts have been made on the sensor side. For instance, the low noise efficiency factor (NEP) and wideband polymer microring resonators are used in the PA imaging to improve the sensitivity of the ultrasound transducers [4]. In addition, on the target side, different external imaging contrast agents are injected, which can increase the optical absorbance and thermoacoustic conversion efficiency [5], [6], [7]. Moreover, to focus the light on media, the nonlinear photoacoustically guided wavefront shaping technology is developed in [8]. A variety of non-linear effects, including the Grueneisen-relaxation based nonlinearity, reversible-switching-based nonlinearity, absorption saturation-based nonlinearity, thermal-based nonlinearity, resolution-dependent nonlinearity, are also used to improve the PA imaging performance [9], [10], [11]. However, few efforts are made in the readout circuits and systems for the sensitivity improvement.

The size and power consumption are two other significant challenges because the PA imaging system is undergoing a revolution towards portable and wearable applications [12], [13], [14]. As shown in Fig. 1, the traditional PA imaging systems include a pre-amplifier to enhance the detected PA pulses, a filter to suppress the out-of-band noise and an analog-to-digital converter (ADC) to obtain the digital output for signal processing. The circuit modules are always bulky and unportable, for instance the Olympus amplifier (76 $\times$51$\times$ 127 mm^3) and wave runner 9000 oscilloscope (358 $\times$ 445 $\times$ 242 mm^3) which are widely used as the
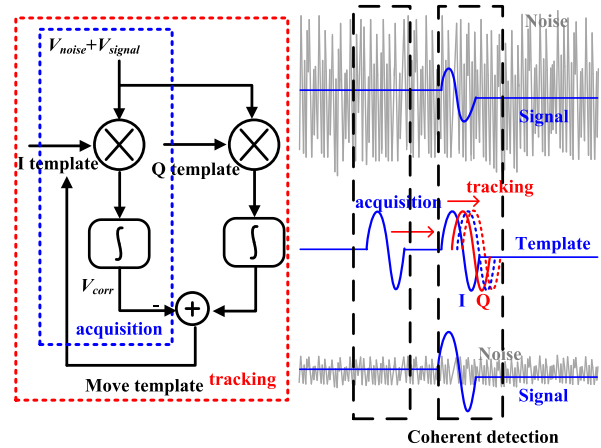
pre-amplifier and analog to digital converter in PA imaging systems. A more compact data acquisition module is developed in [15] which is implemented by off-the-shelf elements and includes 32 channels. However, the system is still bulky. Analog front-end (AFE) chips, for instance the AFE5816, were developed by the TI Inc. which make the system much smaller in size. However, the sensitivity is not particularly improved in these system solutions. About 5.5μV sensitivity is achieved due to the power consumption limitation.

Based on the above elaboration of the PA imaging system, four main contributions are made in this work. (a) We presented a newly implemented and complete PA imager which achieves the highest sensitivity than state-of-the-arts. A preliminary concept and implementation of the new PA imaging receiver was proposed in [16]. In the receiver, the mixed-signal coherent detection (MS-CD) technique is proposed to enhance the output signal-to-noise ratio (SNR). (b) Through the early-late tracking algorithm, the receiver can also search and lock into the location of weak PA pulses which are even immersed in noise. (c) A complete receiver system is integrated on a single chip, leading to a much smaller dimension of 2.5 $\times$ 2.8mm^2. (d) Typically, in the front-end of the ultrasound imaging receivers, the power matching technique is generally employed [17] to improve the output amplitude of the transducers. However, it cannot minimize the noise figure (NF) of the receiver front-end system. Thus, the resonant noise matching (RNM) technique is proposed in the receiver to enhance the sensitivity further [18]. Finally, comparing to the beamforming receivers using tens to hundreds of channels, only 4 channels are employed in this work which are used to suppress the dispersity because of PA scattering of PA signals.

The paper presents the system as follows. Section II introduces the coherent detection and the early-late algorithm. Thereafter, the system architecture of the proposed receiver is illustrated in Section III. Then, Section IV brings the details of the circuit blocks. Then, Section V provides the testing results of the system and circuits. Finally, the conclusion is given in Section VI.
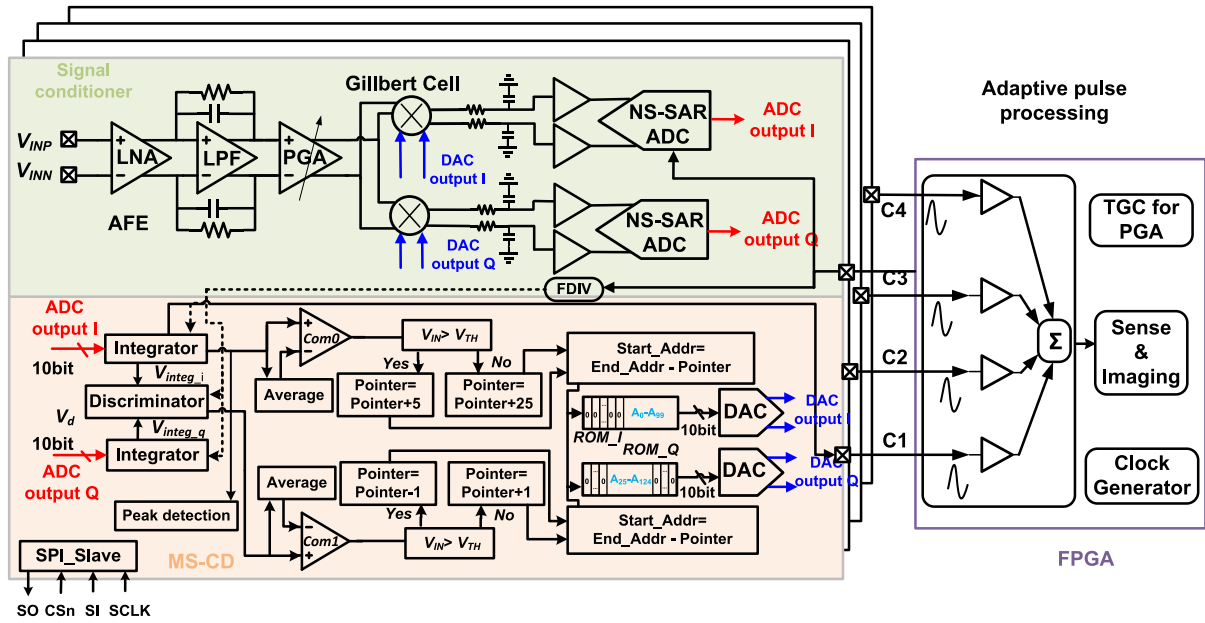
FIGURE 3. System diagram of the receiver SoC.

II. THEORY OF THE MS-CD RECEIVER

In the long-range communication systems, the coherent detection technique is widely employed to extract the weak desired signals from noise [19]. Through correlating with a specific template signal, the received signal $s(t)$ is enhanced while the noise $n(t)$ is suppressed. Thus, the output SNR is improved. As the deep *in-vivo* PA signal is also weak and noisy due to the attenuation and scattering in tissues, the coherent detection technique is considered to boost the SNR and improve quality of the image. The working principle of the proposed coherent detection is shown in Fig.2. The maximum amplitude of the PA pulse can be found when it is aligned with the template.

As mentioned, a template signal which is high correlated with the received PA pulse is required for the coherent detection. To obtain such a template, the identical laser and ultrasound transducer as in the real imaging system are needed. Then the laser illuminates to a target which can absorb most energy and convert to a strong ultrasound signal. Furthermore, to reduce the noise in the template, multiple tests can be conducted, and the output can be averaged.

As the correlation algorithm needs to search the effective PA pulses in a long pulse repetition interval (PRI) of the laser shooting, the scanning time for an image will be prolonged. To solve this problem, the early-late acquisition and tracking technique is used in this work to search the PA pulse automatically and track the pulse steadily. Through moving the template signal close to the PA pulse, the early-late technique can lock the pulse's location.

The early-late searching contains two steps: the acquisition and the tracking. In the acquisition process as shown in Fig.2, the correlation results will be compared with a threshold voltage V_{th} to determine staying in this phase or continue.

The V_{th} is acquired by assessing the background noise of the system. If $V_{corr} < V_{th}$, the templates move forward along the time index to approach the PA pulse. This process continues until $V_{corr} > V_{th}$, then the acquisition finished. As the acquisition is employed to find the PA pulse's rough location, the searching step is generally large and runs over a long PRI. To lock the template to the PA pulse, the tracking phase is needed which requires in-phase (I) and quadrature (Q) templates. The I and Q templates will do correlating calculation with the PA pulse respectively. Then the relationship between the two correlation results will be judged through a discriminator. Finally, the output of the discriminator will determine the templates moving forward or backward. If the discriminator output is positive, the I and Q templates will move forward, otherwise, both move backwards. When the two correlation values are identical, the templates stop moving. In this way, the close loop tracking can search and lock to the location of the PA pulse automatically. And the detection probability is expressed as [20]:

$$P_d\left(V_{th}\right) = Q_m\left(\sqrt{\frac{\lambda}{\sigma_n^2}}, \sqrt{\frac{V_{th}}{\sigma_n^2}}\right), \qquad (1)$$

where the Q_m is the Marcum Q-function, the λ and σ_n^2 are the mean value and the variation of the received signal.

III. IMPLEMENTATION OF THE SYSTEM

The system diagram of the proposed receiver is shown in Fig. 3. In the system, the AFE is designed to enhance the wanted PA pulse and suppress the noise. In addition, the MS-CD is implemented through the Gilbert cell, ADC, digital-to-analog converter (DAC) and the digital circuits. To optimize the sensitivity of the receiver, the input-referred
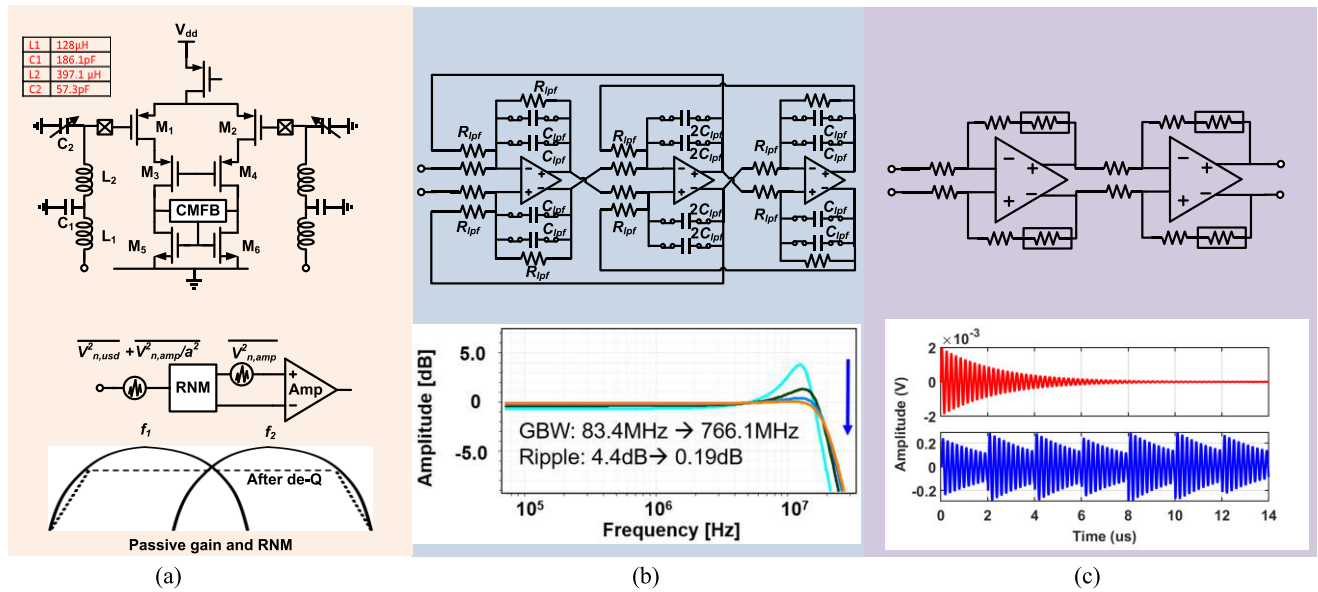
FIGURE 4. Diagram of the (a) LNA with RNM, (b) LPF and (c) PGA.

noise of the AFE is controlled at about 4μVrms in 10MHz bandwidth (BW). In addition, the AFE achieves a variable gain of 0dB to 72dB to adjust the amplitude of the PA pulse. The ADC accomplishes 66dB dynamic range (DR). In order to implement the coherent detection technique, the PA pulse is firstly multiplied with the template signals through the analog multiplier. The template signals are obtained in advance and stored in the read-only memory (ROM). Then the products feed into the ADC. Thereafter, the products are integrated in a certain time window by the digital accumulator. After that, the template in I path is shifted according to the relationship between V_{corr} and V_{th}. When the signal is acquired, the relationship between the integration results in I and Q paths is judged by a discriminator. Eventually, the I and Q templates are moved according to the discriminator's output. Through the analog multiplying, digital integrating and the templates' moving in timeline, the cross correlation is realized. In addition, the PA pulse is locked by the templates which is moved in early-late method.

IV. CIRCUIT IMPLEMENTATION

The AFE includes a low-noise amplifier (LNA), a 3rd order low-pass filter (LPF) and a programable gain amplifier (PGA) controlled by a time-gain compensation (TGC) circuit. The dynamic range of the echo signals from deep tissue is up to 90 dB because of the attenuation in the propagation paths [21]. The LNA provides 30dB gain to suppress the noise from subsequent stages. And it will be by-passed when the incoming signal is larger than 14mV which is the 1-dB compression point. As the main target of this design is to process weak PA signals from deep tissue, the LNA is hand-tuned in this prototype. The input-referred noise density is about 1.3nV/$\sqrt{\text{Hz}}$@5MHz. The LPF with a BW of 10MHz is used to reduce the out-of-band noise and unwanted interferences. The PGA can provide 0-42dB variable gain. An oversampling

successive-approximation register (SAR) ADC with noise shaping (NS) [22], [23] is employed to convert the PA pulse to digital signal. Thick gate transistors working at 1.8V voltage are used in the AFE for a large DR while the core transistors working at 1V are used in the ADC and DAC for high speed. A 10-bit current steering DAC is adopted to form an analog PA template pulse.

A. ANALOG FRONT-END

The LNA is connected to the transducer directly in an ultrasound receiver, thus, its NF must be minimized. The dominant noise in the receiver comes from the circuit components, the power supply, and the substrate which can couple the digital signals [24], [25]. Thus, the isolation of the digital circuits and analog circuits in layout is highly desired. In addition, the noise generated during photoacoustic energy conversion is also significant, including thermal acoustic noise due to conversion from thermal energy to mechanical expansion in the medium, and thermal noise because of conversion from PA pulse to electrical signal in the ultrasonic transducer.

The LNAs which are connected to capacitive micromachined ultrasonic transducer (CMUT) generally use trans-impedance amplifier (TIA). However, as the piezoelectric transducer (PZT) used in this work has lower output impedance and mainly delivers voltage signals, operational trans-conductance amplifier (OTA) attracts more attention than the TIAs. Consequently, the common-source amplifier with high input impedance is selected to extract the voltage signal converted from the transducer. Single-ended inverter-based OTAs can improve the power efficiency by superimposing the trans-conductance of N-channel metal-oxide semiconductor (NMOS) and P-channel metal-oxide semiconductor (PMOS) transistors, but it has large current changes caused by power-voltage-temperature (PVT) variations, as well as poor power supply noise rejection. Thus, the

differential architecture is selected. Furthermore, as the working frequency of the ultrasound transducer can be low to hundreds kHz, output SNR deterioration caused by flicker noise may be more serious than the thermal noise. Typically, PMOS transistors have lower 1/f noise corner frequency than NMOS. Thus, PMOS transistors can behave much better on noise performance than the NMOS transistors. The input-referred voltage noise of the LNA in Fig.4(a) can be expressed as:

$$\overline{V_{ieq}^2} = \overline{V_{5n}^2}\left(\frac{g_{m5}}{g_{m1}}\right)^2 + \overline{V_{1n}^2}. \tag{2}$$

The noise from the cascode transistor M_3 is mitigated by the intrinsic gain of the input transistor M_1. The noise of the loading transistor M_5 is also reduced by g_{m1}. Thus, with the same current, the $(W/L)_1$ is designed much larger than the $(W/L)_5$. The digital circuits bring considerable distortion to the analog circuits on the same die through the parasitic resistance R_{bp} and capacitance C_{bp} in substrate. In addition, thermal noise is also caused by the R_{bp}, which can be described as:

$$\overline{I_{n,sub}^2} = g_{mb}^2 \times \overline{V_{n,sub}^2}, \tag{3}$$

$$\overline{V_n^2} = \frac{\overline{I_{n,sub}^2}}{g_m^2} = \frac{g_{mb}^2}{g_m^2} \times \overline{V_{n,sub}^2}. \tag{4}$$

To reduce the input-referred noise further, the RNM technique is employed in the LNA as shown in Fig.4 (a). The RNM transfers the output impedance of the transducer to high impedance and realizes passive gain. As the passive gain is provided by passive elements, the RNM can reduce the input-referred noise of the LNA without consuming any power and bring negligible noise. The working frequency of the RNM network are first evaluated according to the upper and lower cut-off frequency of the transducer. Finally, the parameters of the RNM network are confirmed with the aid of advanced design system (ADS) software. In addition, a degrading quality factor (de-Q) resistor is used to make the in-band gain flat. Besides the in-band passive gain, the RNM also provides out-of-band attenuation which reduces the noise further. Through this technique, the output SNR of the LNA is enhanced by about 5dB.

After the LNA, the PA pulse goes through a 3rd-order LPF as shown in Fig.4(b). The Butterworth topology is selected because it can provide maximally flat amplitude within the passband and moderate phase distortion comparing with the other topologies (Chebyshev, Bessel and Elliptic). The 3rd-order Butterworth LPF implemented by LC components is first synthesized. The inductors in the filter are then replaced by active integrators based on the Kirchhoff's current law (KCL) and Kirchhoff's voltage law (KVL) [26].

The bandwidth of the filter is determined by $1/(2\pi R_{lpf} C_{lpf})$. If the capacitor value is too big, the loading of the operational amplifier (OPA) is large which will lead to high power consumption. If the capacitor is too small to satisfy that C_{lpf} is much larger than the input parasitic capacitance of the OPA, the signal will be attenuated in the filter. As known, one
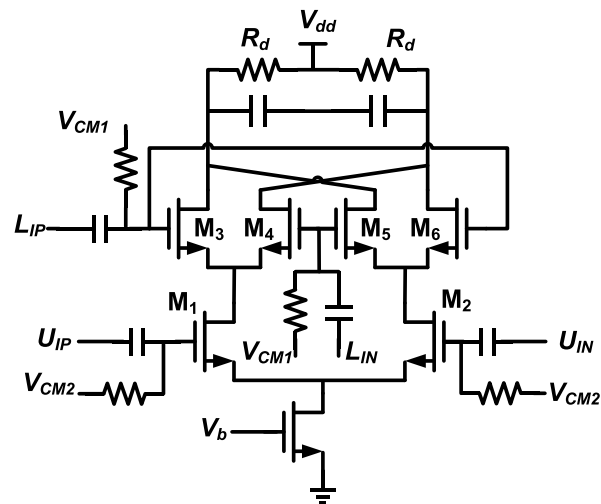

FIGURE 5. Schematic of the multiplier.

real pole and one pair of imaginary poles exist in the 3rd order Butterworth filter with a transfer function of:

$$H(S) = \frac{1}{1 + 2s + 2s^2 + s^3}. \tag{5}$$

The poles are: -1 and $-0.5 \pm 0.866i$. For the pole at -1, the capacitor value of the middle integrator can be determined by: $f_c = \frac{1}{2\pi R_{lpf} C_{lpf}}$.

As the roll-off of a LPF is caused by the R_{lpf} and C_{lpf}, the real part of the pole represents the loss of the filter. Thus, when the resisters are identical, the ratio of the capacitors at different integrators is equal to the ratio of the real part in the poles. For the poles at $-0.5 \pm 0.866i$, the capacitor value can be calculated as:

$$0.5 \times f_c = \frac{1}{2\pi R_{lpf} C_{middle}}, \quad C_{middle} = 2C_{lpf}. \tag{6}$$

By this means, the odd order Butterworth filters can be designed. Firstly, the value of the capacitor C_{lpf} in the middle integrator can be obtained according to the cut-off frequency of the filter. Then for other capacitors, the value can be obtained through multiplying the real part of the pole by C_{middle}.

The ΔQ_{LPF} representing the quality factor variation of the Butterworth filter due to the non-ideality $\Delta(s)$ can be obtained by:

$$\Delta(s) = \frac{s^2 R_{lpf} C_{lpf}}{GBW}, \tag{7}$$

$$\Delta Q_{LPF} = \frac{s^2}{\Delta(s) GBW^2}. \tag{8}$$

From the equations, we can see that the non-ideal factor $\Delta(s)$ affects the AC response of the filter. Moreover, the $\Delta(s)$ is affected by the gain bandwidth product (GBW) of the OPA. As the gain of the OPA is generally finite, and the bandwidth is also limited by power consumption, the transfer function of the filter is affected by these non-ideal factors [27].

The schematic of the active-RC filter is shown in Fig.4(b). Three amplifiers are required in the filter. The GBW of the
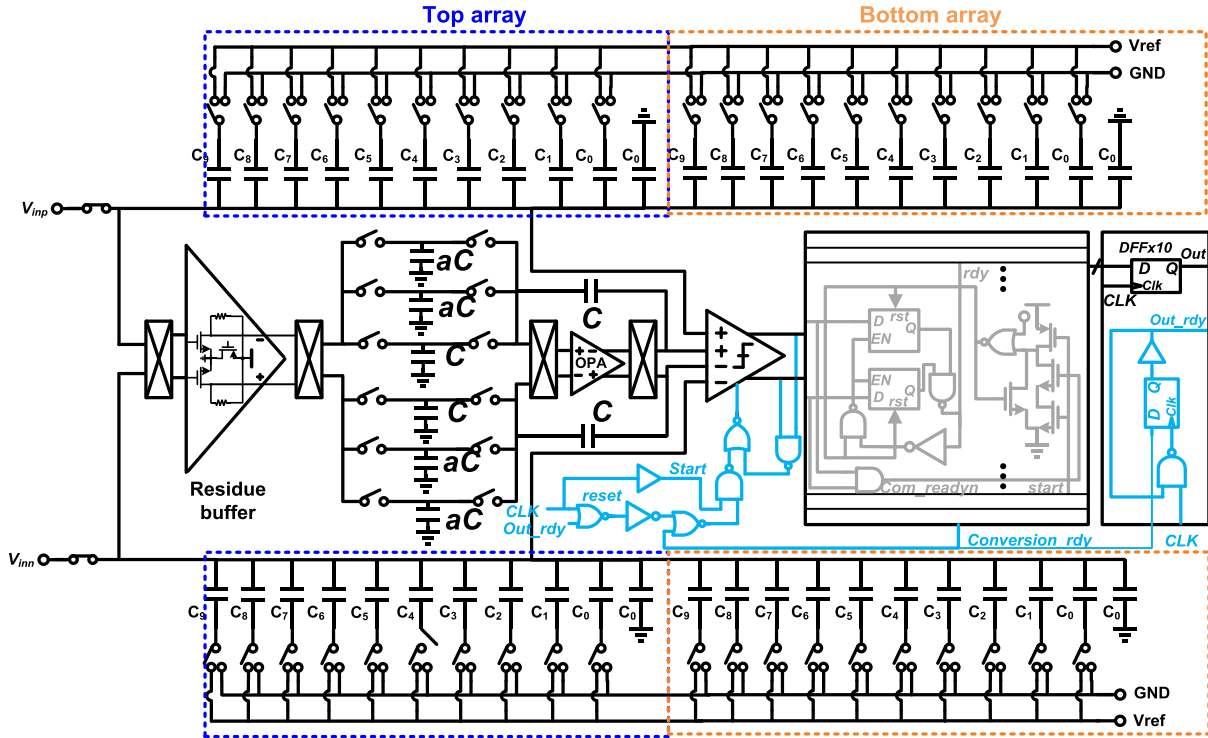
FIGURE 6. Schematic of the NS-SAR ADC.

OPAs need to be about 100 times of the filter's cut-off frequency to make the Q_{LPF} variation negligible as discussed in (8). Such a high *GBW* will bring high power consumption. On the other hand, as the capacitor value of the middle integrator is twice of that in the side integrators, the *GBW* of the OPA in the side integrators is half of that in the middle OPA [28], [29].

Because of the light scattering and energy attenuation in the propagation path, the echoes from skin could be much stronger than the wanted echoes from the internal organizations. Therefore, a PGA circuit, which can provide a dB-linear gain ranges from 0 to 42 dB with 6 dB step, is implemented to cover the dynamic range requirement [30]. The schematic is shown in Fig.4(c). The gain control signal of the PGA which increases from 0000 to 1111 during one PRI is provided by the FPGA. With the ultrasound speed of 1500m/s in tissue, the time needed to travel from the skin to the target at 10mm is about 6.7μs. The input and output of the PGA with TGC are shown by the red and blue waves respectively.

B. MIXED-SIGNAL COHERENT DETECTOR

The coherent detection includes two main steps, the multiplication and integration, which are implemented in the analog domain and digital domain respectively. The multiplier is implemented by a differential Gilbert cell as shown in Fig. 5. The cut-off frequency of the AC coupler is about 100kHz which is determined by the working frequency of the transducer. The output of the multiplier can be calculated as:

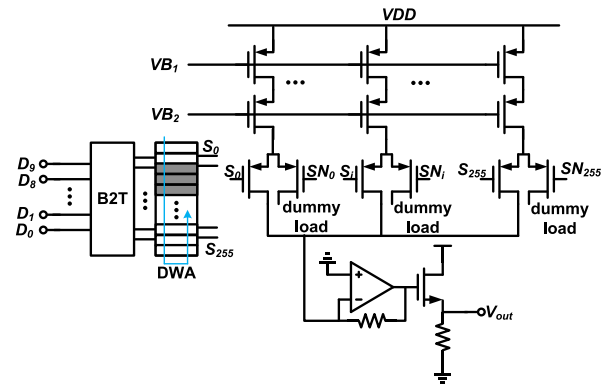$$V_{out} = \sqrt{2KK_1}V_{template} \times V_{ultrasound}R_d, \quad (9)$$

FIGURE 7. Schematic of the DAC.

where $K = \mu_n C_{ox}(W/L)_{1,2}$, and $K_1 = \mu_n C_{ox}(W/L)_{3,4}$. It achieves 20MHz bandwidth with about 10dB gain from U_{Ip}/U_{In} to the output. Considering the tradeoff between linearity of the multiplier and the SNR enhancement of the MS-CD, the amplitude of 200mV is selected for the template signal. The output of the multiplier is finally digitized by the ADC. An anti-aliasing filter is implemented with passive elements prior to the ADC to attenuate the high order product of the multiplier.

As the interface of the analog and digital part of the whole receiver, the ADC plays a crucial rule. And its dynamic range, speed, and SNR determine the overall performance and the reliability of the system. Moreover, the SAR ADC topology is employed because the imager needs low power consumption for wearable and flexible applications. Additionally, to reduce the quantization error to the level below circuits
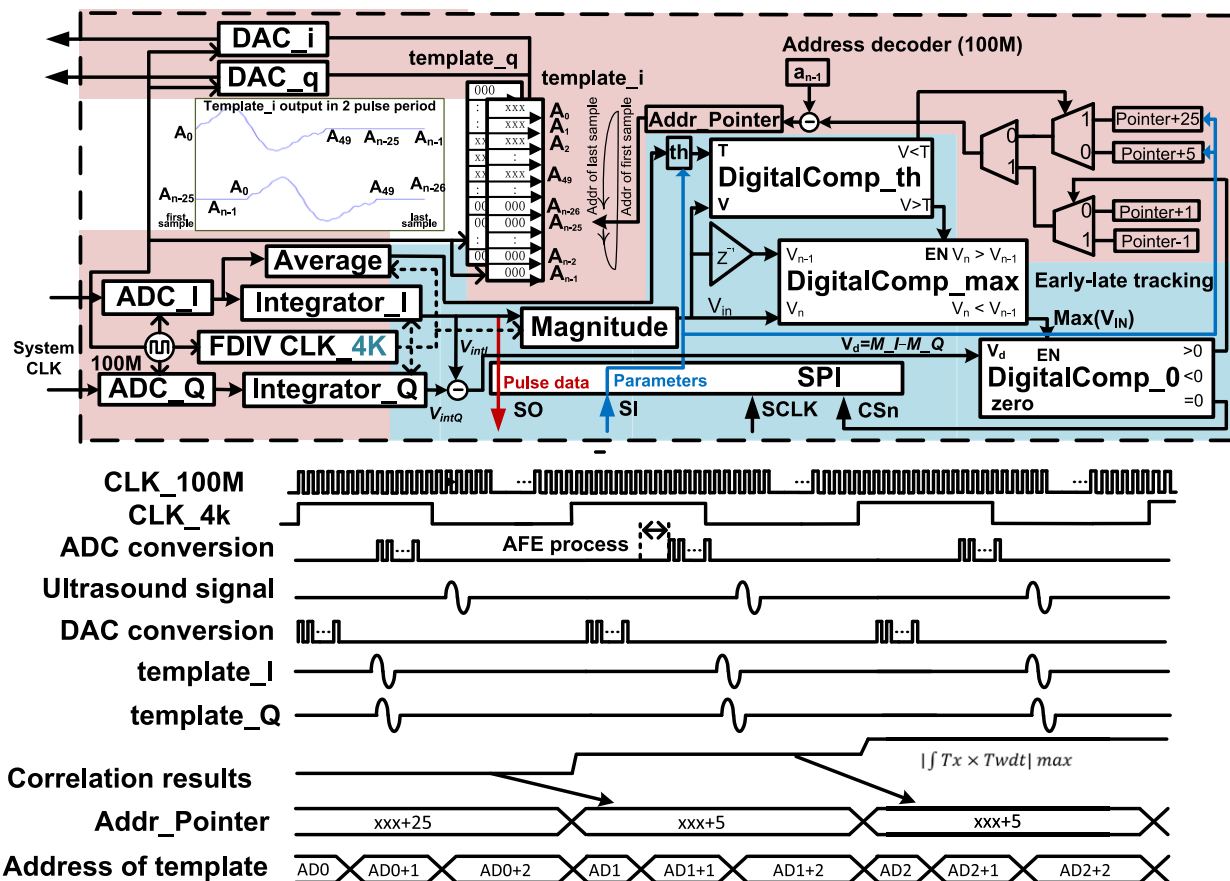
FIGURE 8. Digital circuit diagram and signal flow of coherent detection.

noise of the system, oversampling SAR ADC is implemented. To increase the output SNR of the ADC further, NS technique is employed. Consequently, the sampling rate of 100MSps is selected in the ADC, leading to 10ns time resolution for digital signal processing. 100 sampling points are used in the integration for coherent detection. Notably, the bandwidth of the ADC is 10MHz which can cover the working frequency of the transducer. Furthermore, 70.3dB spurious-free dynamic range (SFDR) is achieved to ensure the linearity of the system.

The asynchronous timing scheme (ATS) is adopted in the ADC for high sampling rate of 100MSps. In addition, the ATS also makes the ADC easily enable when a trigger signal comes. The architecture of the ADC is shown in Fig. 6. To ensure that the kT/C noise is lower than the noise requirement of the ADC, the sampling capacitor is selected as 2.56 pF, leading to a least significant bit (LSB) capacitor of 2.5fF. The split capacitor array architecture is employed in the DAC to reduce the switching energy while keeping the common-mode voltage unchanged. To ensure the linearity of the ADC, bootstrap switches are employed.

The SAR logic circuits are shown in Fig. 6. There are 10 control slices for a 10-bit conversion. Initially, during sampling, the outputs of the comparator are reset to high which results in $Com\_readyn = 1$. In addition, the reset signal is high before conversion. After one sampling, the
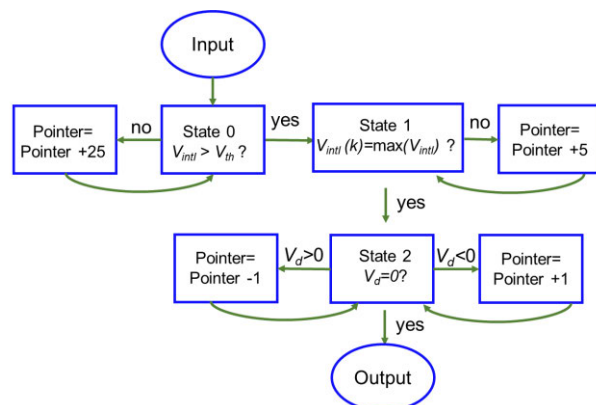

FIGURE 9. Flow chart of the early-late algorithm.

start signal following the sampling clock feeds into the most significant bit (MSB) control slice. Consequently, the latch is enabled because the EN signal turns to high. The start signal also enables the first comparison of the comparator. Then the outputs of the comparator for the MSB comparison are latched when arriving the SAR logic circuits. Thereafter, the ready signal rdy feeds back to the NAND gate and disables the latch to block the following results of the comparator. Simultaneously, the rdy signal also works as the start signal of next control slice. When the comparator is reset, the latch of next control slice is enabled. Like the previous conversion, the comparison results are latched and then transferred to

the DAC. The process continues until the LSB is output to the DAC and the conversion ready signal is generated. The output ready signal is generated after the *Conversion_ready* turns to high. Ultimately, the reset signal for the SAR logic is produced.

For the noise shaping technique, the finite impulse response (FIR) circuit is connected to the DAC output. The FIR input buffer is used to amplify the residue signal of the ADC. However, during the time of one conversion, the DAC's output will change from the sampled signal to a residue signal. Such a big variation will affect the input capacitance of the buffer. Consequently, the varying input capacitance of the residue buffer will generate non-linearity to the ADC. Thus, before the conversion is done, the buffer should be shut down. As shown in Fig.6, the differential outputs and the common source node will be shorted to the power supply. Then the input differential pair will be turned off and the input parasitic capacitance will be controlled with negligible effect. In addition, the residue signal attenuation due to charge redistribution is also acceptable because the common-mode input capacitance is much smaller than the sampling capacitor. The transfer function of the ADC is expressed as:

$$D_{out}(z) = V_{in}(z) + \frac{1-z^{-1}}{1+z^{-1}+2/3z^{-2}}(Q_{ADC}(z)$$
$$+ V_{n,com}(z)) + \frac{2z^{-1}+2/3z^{-2}}{1+z^{-1}+2/3z^{-2}}V_n. \quad (10)$$

The $Q_{ADC}(z)$ and $V_{n,com}(z)$ represent the quantization noise and the comparator's noise respectively which are moved to high frequency and filtered by digital circuits. V_n represents the input-referred noise of the filter cascaded by FIR and infinite impulse response (IIR) filters. The choppers are used to move the noise V_n to out-of-band. Comparing to the traditional multi-bit $\Delta\Sigma$ ADCs, the NS-SAR architecture reused the DAC for SAR conversion and residue processing [31]. In this way, the silicon area can be saved.

The schematic of the DAC is shown in Fig. 7. The binary input is firstly converted to the thermometer code to reduce the differential non-linearity. Furthermore, the data weighted averaging (DWA) technique is employed to remove the in-band distortion [32]. Cascode current source is used to increase the current accuracy and immunity to the output voltage noise. The current of one LSB is 1μA and the total current is 1024μA. The size of the transistors is selected according to the tradeoff between the output current accuracy and leakage. Because the large transistor size is beneficial to output accuracy, but it also increases the leakage. Consequently, the Monte Carlo simulation is used to select the optimum size of the transistors. A transimpedance amplifier is implemented to convert the current to voltage. Considering the output SNR of the DAC, the noise of the OPA is designed to be about 20μVrms.

Fig.8 demonstrates the digital IC system which is used to capture and track the PA pulse from the transducer. To ensure that the ADC, DAC and the digital circuits can work synchronously, a master clock is generated from FPGA.
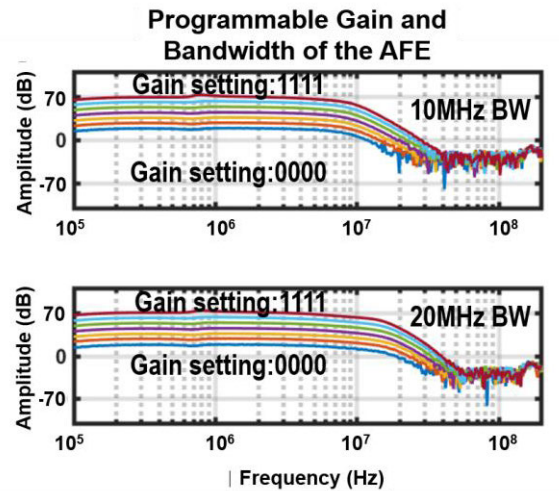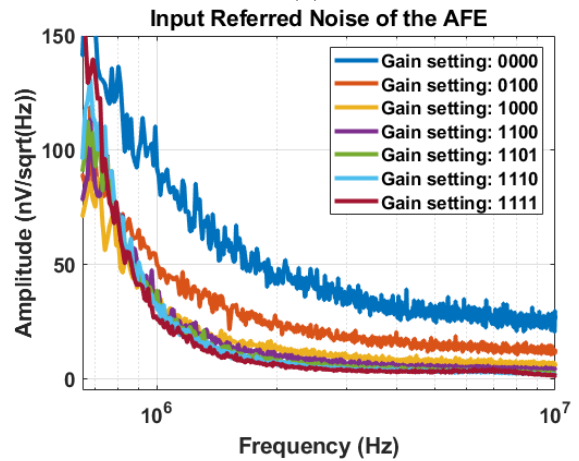
FIGURE 10. Measurement results of (a) gain and bandwidth, (b) input-referred voltage noise density of the AFE.
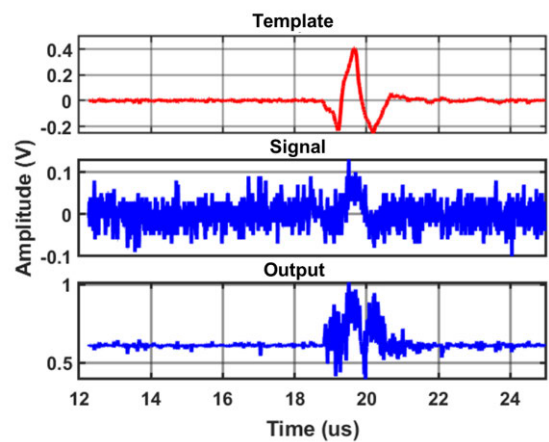

FIGURE 11. Measurement results of the multiplier.

The system clock is 100MHz. ROM_I and ROM_Q store 100 points of template pulse, zero padding fills in the rest memory to simulate the real pulse in one period. Two samples in the ROM are converted to analog signals by the DACs, then they multiply with the incoming PA pulses in analog

domain. Subsequently, the ADCs convert the multiplication results into digital signals. After that, integrators accumulate the ADCs' output in one pulse period. The frequency divider (FDIV) divides the 100MHz system clock into 4kHz for the acquisition operation. V_{intI} represents the correlation result between the template pulses and PA pulses. After each capture cycle, the integrators will be cleared for next pixel's operation.

The two-step early-late searching is described by the flow chart in Fig.9 firstly. There are 3 statuses in the processing. During the acquisition and tracking, the template pulses converted from the ROM need to be moved along time index. Thus, the pointer of reading the templates is shifted in every PRI. In the acquisition process, the pointer is decoded based on V_{intI},

$$V_{intI}(k) = \sum_{25(k-1)}^{25k+74} V_{adcI}(n), \qquad (11)$$

where the k is the PA pulse number, and the n represents discrete time point. Firstly, in status 0, the $V_{intI}(k)$ is taken into DigitalComp_th and compared with V_{th}, which is related to the average energy of background noise. If $V_{intI}(k) < V_{th}$, the correlation result is 0. Therefore, the pointer needs to plus 25. Then 25 zero paddings are inserted before the template pulse. Accordingly, the template pulse is shifted forward by a quarter of one period to approach the incoming PA pulse. This process will be repeated until the template signal and PA pulse overlap, which results in $V_{intI}(k) > V_{th}$. Since then, as shown in status 1, DigitalComp_max is started to detect the peak of V_{intI}. In this phase, the searching step is reduced to 5, and the template pulse will shift 5 points forward. In this phase,

$$V_{intI}(k) = \sum_{5k+20k_0-5}^{5k+20k_0+94} V_{adcI}(n), k > k_0, \qquad (12)$$

where k_0 is the number of pulses in status 0. The $V_{intI}(k-1)$ is saved and will compare with $V_{intI}(k)$ until $V_{intI}(k-1) > V_{intI}(k)$. Then the peak $V_{intI}(k-1)$ is detected, and the PA pulse is captured.

The output signal from DigitalComp_max when $V_{intI}(k-1) > V_{intI}(k)$ triggers the early-late tracking loop in status 2. The $V_d(k) = V_{intI}(k) - V_{intQ}(k)$ represents the difference between the output of integrator_I and the output of integrator_Q.

$$V_{intI}(k) = \sum_{24k_0+4k_1+k-1}^{24k_0+4k_1+k+98} V_{adcI}(n), k > k_0 + k_1, \qquad (13)$$

$$V_{intQ}(k) = \sum_{24k_0+4k_1+k-1}^{24k_0+4k_1+k+98} V_{adcQ}(n), k > k_0 + k_1, \qquad (14)$$

where k_1 is the number of pulses in status 1. The comparison between V_d and 0 will be processed in DigitalComp_0. Then the comparison results feedback to the ROM and push
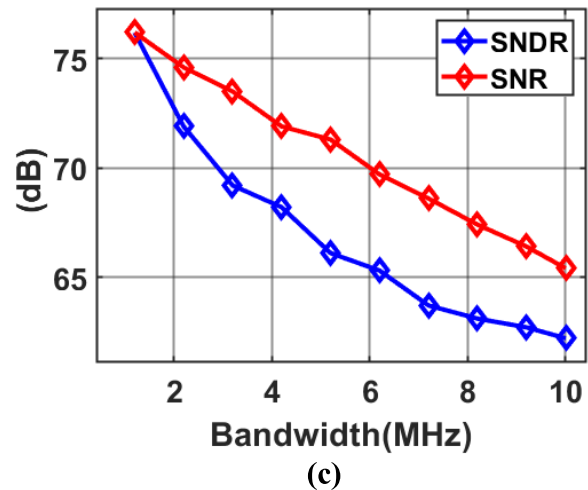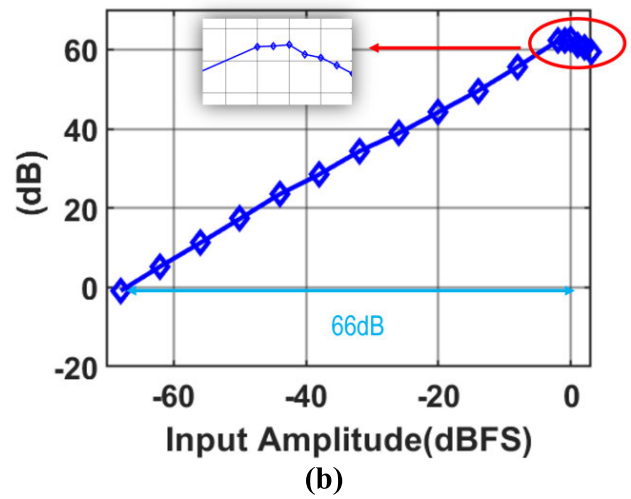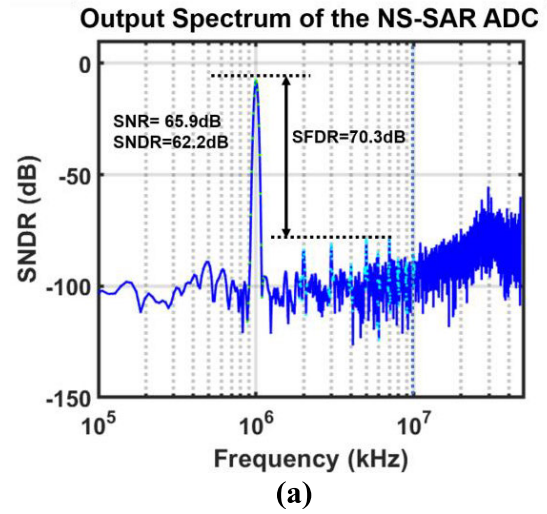

(a)

(b)

(c)

FIGURE 12. Measurement results of (a) spectrum, (b) dynamic range and (c) SNDR and SNR v.s BW of the ADC.

the template pulses forward or backward by one point. The tracking procedure continues until $V_d = 0$ when the PA pulse is locked. Finally, the results of integrator_I are transferred to master in slave out (MISO) port of the SPI. The parameters
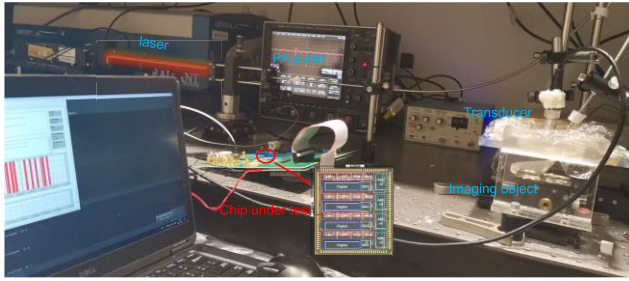
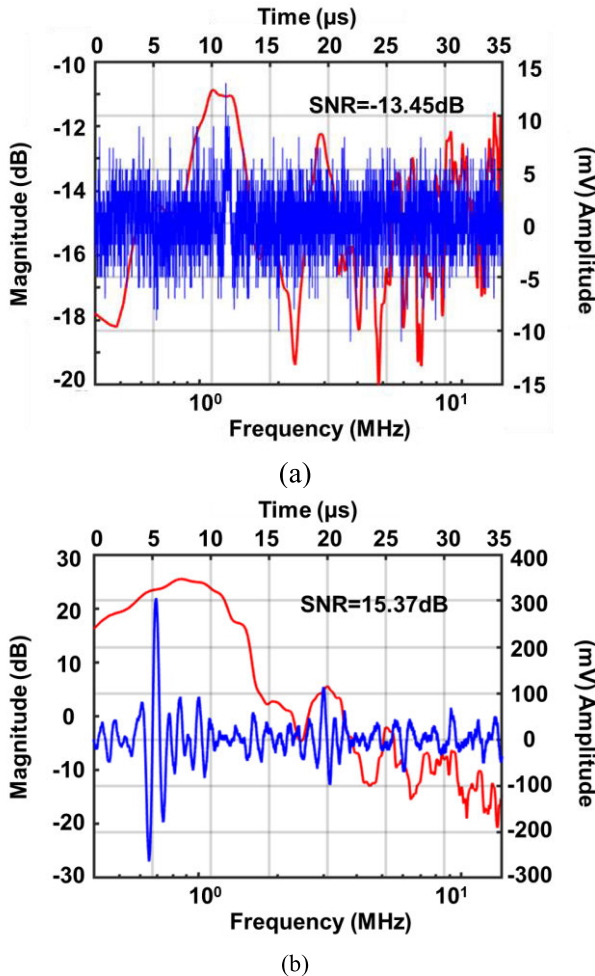**FIGURE 13.** Setup of the photoacoustic imaging.

(a)

(b)

FIGURE 14. Measurement results of the PA pulse (a) without coherent detection and (b) with coherent detection.

in the digital system, such as the searching steps of 25 and 5, can also be programmed by SPI.

V. MEASUREMENT RESULTS

The proposed PA receiver ASIC is fabricated in 65nm 1P9M CMOS process. The area of 4 channels is about 5.7 mm^2. The layout of the analog part is isolated from the digital part to weaken the noise in substrate. The power supplies of the AFE, the ADC, DAC and digital circuits are separated. The power consumption of a single channel is 28.8 mW.

The LNA is tested separately from the SoC chip. The RNM network implemented with off-the-shelf elements provides about 5dB passive gain. Therefore, the noise performance
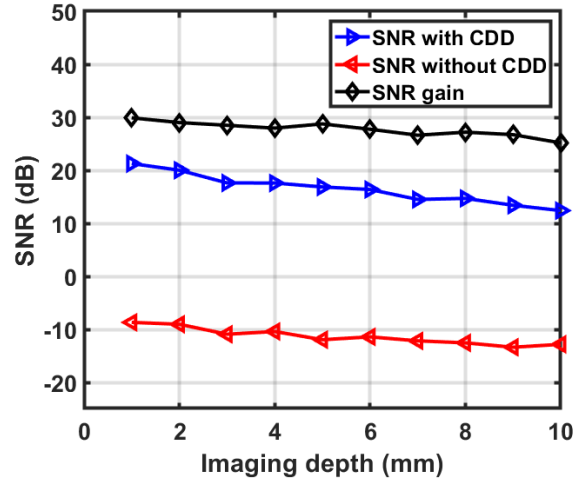

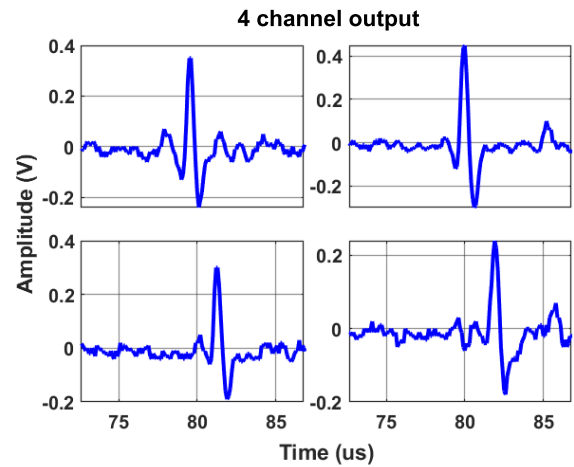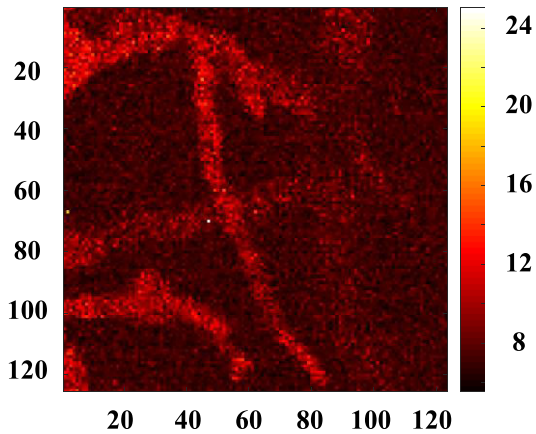**FIGURE 15.** Measurement results of detection SNR enhancement v.s. depth.

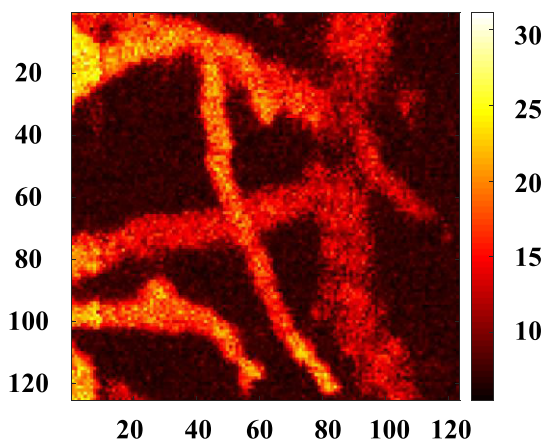**FIGURE 16.** Testing results of the 4 channels receiver.

requirement of the LNA is relaxed, and hence the power consumption is reduced by about 1.5 times. Consequently, the LNA with RNM achieves 1.3nV/$\sqrt{\text{Hz}}$ input-referred noise with 3mW power consumption. When interfacing with a transducer with 10μV/Pa efficiency, the LNA achieves a low NEF of 0.23mPa$\sqrt{\text{mW/Hz}}$.

The measured results of the AFE are shown in Fig. 10. The gain of the AFE can be programmed from 30dB to 72dB with 6 dB step. In addition, the bandwidth can be tuned from about 10 MHz to 20MHz, which are shown in Fig.10(a). The input-referred noise of the AFE is about 4.3μVrms under the maximum gain of 72dB to ensure the superior sensitivity of the receiver. The circuit noises density of the AFE at different gains are shown in Fig. 10(b). Transient testing results of the multiplier are shown in Fig.11.
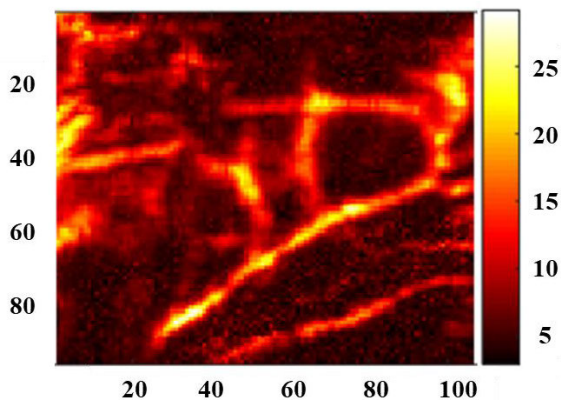
The electrical performance of the NS-SAR ADC is also evaluated. The sampling rate is 100MSps. The input to the ADC is a 1 MHz and 1 V$_{pp}$ sinewave signal from a RF signal generator. Then the output data is collected by a logic analyzer. Thereafter, the output spectrum is calculated in MATLAB and shown in Fig. 12(a). The SNR in 10MHz is

(a)

(b)

(c)

FIGURE 17. Photoacoustic imaging results of the phantom (a) with traditional receiver, (b) with MS-CD receiver, and (c) vessels.

TABLE 1. Comparison with the state-of-the-art work.

	This work	JSSC'17 [21]	ISSCC'18 [33]	ISSCC'20 [34]	ISSCC'18 [35]
Process	65nm	28nm	180nm	180nm	180nm
DR (dB)	138	90	80	--	--
BW (MHz)	10	10	10	7	11.2
Max gain	72dB	71dBΩ	48dB	106dBΩ	32dB
Input-referred Noise	4.3 μVrms	238.1 μVrms	18.6 μVrms	5.3 nArms	15.4 μVrms
Power consumption (mW)	28.8/per channel	280	131	313.6	400.6
*Sensitivity	0.15 μVrms	58.9 μVrms	1.55 μVrms	0.66 nArms	1.92 μVrms
**SNR gain (dB)	28.9	12.0	21.6	18.1	18.1

* Sensitivity is calculated when the input SNR=0dB.
** SNR gain of the receivers with beamforming is calculated according to $10\log_{10}M$.

To demonstrate the SNR enhancement of the proposed receiver, PAI experiments are conducted with the setup in Fig. 13. A fiber laser with 750nm wavelength is employed as the light source. The output fluence is about 1mJ/cm² which is much lower than the ANSI safety standard [33]. A phantom is used as the imaging object, which is placed in water for ultrasound matching. An ultrasound transducer is fixed in a holder together with the laser fiber to generate a stable and homogenous overlap between the optical filed and transducer's focus point. The SNR improvement is preliminarily verified by the testing results in Fig.14 which shows the transient signal and the spectrum of a single pixel. When the MS-CD is not used, the signal is almost immersed in noise and the SNR is only −13.45dB. After enabling the MS-CD, the signal can be clearly observed, and the SNR is improved to 15.37dB. Consequently, 28.9dB SNR increasement is achieved, leading to a sensitivity of 0.15μVrms. As the performance of coherent detection could be degraded by the non-Gaussian noise, the PA signals at different depth are measured and analyzed. The results are shown in Fig.15. At the depth of 10mm, the SNR improvement maintains at 25dB. To collect the reflected ultrasound wave in all directions, the other 3 channels can be enabled to achieve diversity gain. Fig.16 shows the transient outputs of the 4 channels.

Other than testing on a single pixel, the imaging of the phantom is conducted. At the depth of about 1cm, the image cannot be visualized when using traditional PA receiver as shown in Fig.17(a). Whereas when enable the coherent detection technique, as exhibited in Fig.17(b), the image is clearly constructed, and the contrast-to-noise ratio (CNR) achieves 44dB. To further demonstrate the capability of the receiver, an image of blood vessel is tested as shown in Fig.17(c). In addition, as shown in Table 1, the MS-CD technique contributes the highest SNR gain, as well as the best sensitivity when consuming the lowest power consumption.

improved to 65.9dB after enabling the noise shaping technique, resulting in 10-bit effective number of bits (ENOB). Fig. 12(b) portrayed the dynamic range of the NS-SAR ADC. The SNDR and SNR in different bandwidths are shown in Fig.12(c), and 12.3bit ENOB can be obtained in 1MHz bandwidth.

VI. CONCLUSION

Through integrating the coherent detection and early-late tracking techniques, the proposed PA imaging receiver achieves a super sensitivity of 0.15μVrms at 10mm depth. Comparing to the conventional PAI receiver, the output SNR is improved by 28.9dB, and the CNR is enhanced by 23dB. Benefited from the RNM technique, the NEF of the LNA achieves 0.23mPa$\sqrt{\text{mW/Hz}}$ in the working bandwidth of the transducer. An oversampling SAR ADC with noise shaping technique is implemented for higher SNR. Furthermore, the 4-channel receiver is realized in 5.7 mm^2 area and 115.2 mW power consumption, which can achieve 6dB diversity gain for heterogeneous bio-imaging, leading to 6dB SNR improvement.

REFERENCES

[1] G. Ku, X. Wang, X. Xie, G. Stoica, and L. V. Wang, "Imaging of tumor angiogenesis in rat brains in vivo by photoacoustic tomography," *Appl. Opt.*, vol. 44, no. 5, pp. 770–775, 2005.

[2] C. Moore and J. V. Jokerst, "Strategies for image-guided therapy, surgery, and drug delivery using photoacoustic imaging," *Theranostics*, vol. 9, no. 6, pp. 1550–1571, 2019.

[3] S. Mallidi, G. P. Luke, and S. Emelianov, "Photoacoustic imaging in cancer detection, diagnosis, and treatment guidance," *Trends Biotechnol.*, vol. 29, no. 5, pp. 213–221, May 2011.

[4] S.-L. Chen, S.-W. Huang, T. Ling, S. Ashkenazi, and L. Guo, "Polymer microring resonators for high-sensitivity and wideband photoacoustic imaging," *IEEE Trans. Ultrason., Ferroelectr., Freq. Control*, vol. 56, no. 11, pp. 2482–2491, Nov. 2009.

[5] Q. Fu, R. Zhu, J. Song, H. Yang, and X. Chen, "Photoacoustic imaging: Contrast agents and their biomedical applications," *Adv. Mater.*, vol. 31, no. 6, 2019, Art. no. 1805875.

[6] G. S. Sangha, E. H. Phillips, and C. J. Goergen, "In vivo photoacoustic lipid imaging in mice using the second near-infrared window," *Biomed. Opt. Exp.*, vol. 8, no. 2, pp. 736–742, 2017.

[7] Q. Fan, K. Cheng, X. Hu, X. Ma, R. Zhang, M. Yang, X. Lu, L. Xing, W. Huang, S. S. Gambhir, and Z. Cheng, "Transferring biomarker into molecular probe: Melanin nanoparticle as a naturally active platform for multimodality imaging," *J. Amer. Chem. Soc.*, vol. 136, no. 43, pp. 15185–15194, Oct. 2014.

[8] P. Lai, L. Wang, J. W. Tay, and L. V. Wan, "Photoacoustically guided wavefront shaping for enhanced optical focusing in scattering media," *Nature Photon.*, vol. 9, no. 2, pp. 126–132, Jan. 2015.

[9] R. Gao, Z. Xu, Y. Ren, L. Song, and C. Liu, "Nonlinear mechanisms in photoacoustics—Powerful tools in photoacoustic imaging," *Photoacoustics*, vol. 22, Jun. 2021, Art. no. 100243.

[10] X. Liu, T. T. W. Wong, J. Shi, J. Ma, Q. Yang, and L. V. Wang, "Label-free cell nuclear imaging by Grüneisen relaxation photoacoustic microscopy," *Opt. Lett.*, vol. 43, no. 4, pp. 947–950, 2018.

[11] J. Yao, A. A. Kaberniuk, L. Li, D. M. Shcherbakova, R. Zhang, L. Wang, G. Li, V. V. Verkhusha, and L. V. Wang, "Multiscale photoacoustic tomography using reversibly switchable bacterial phytochrome as a near-infrared photochromic probe," *Nature Methods*, vol. 13, no. 1, pp. 67–73, Jan. 2016.

[12] A. Dangi, S. Agrawal, G. R. Datta, V. Srinivasan, and S.-R. Kothapalli, "Towards a low-cost and portable photoacoustic microscope for point-of-care and wearable applications," *IEEE Sensors J.*, vol. 20, no. 13, pp. 6881–6888, Jul. 2020.

[13] T. Kobayashi, T. Islam, M. Sato, M. Ohkura, J. Nakai, Y. Hayashi, and H. Okamoto, "Wide and deep imaging of neuronal activities by a wearable neuroimager reveals premotor activity in the whole motor cortex," *Sci. Rep.*, vol. 9, no. 1, p. 8366, Jun. 2019.

[14] S. Liu, K. Tang, H. Jin, R. Zhang, T. T.-H. Kim, and Y. Zheng, "Continuous wave laser excitation based portable optoacoustic imaging system for melanoma detection," in *Proc. IEEE Biomed. Circuits Syst. Conf. (BioCAS)*, Oct. 2019, pp. 1–4.

[15] C. C. P. Cheung, C. H. Alfred, N. Salimi, B. Y. S. Yiu, I. K. H. Tsang, B. Kerby, R. Z. Azar, and K. Dickie, "Multi-channel pre-beamformed data acquisition system for research on advanced ultrasound imaging methods," *IEEE Trans. Ultrason., Ferroelectr., Freq. Control*, vol. 59, no. 2, pp. 243–253, Feb. 2012.

[16] C. Yang, Z. Fang, X. Tang, X. Lou, K. Tang, and Y. Zheng, "A photoacoustic receiver system-on-chip with a novel correlation detection technique based on early-and-late tracking," in *Proc. IEEE Int. Symp. Circuits Syst. (ISCAS)*, Oct. 2020, pp. 1–5.

[17] A. Ramos, J. L. S. Emeterio, and P. T. Sanz, "Improvement in transient piezoelectric responses of NDE transceivers using selective damping and tuning networks," *IEEE Trans. Ultrason., Ferroelectr., Freq. Control*, vol. 47, no. 4, pp. 826–835, Jul. 2000.

[18] C. Yang, H. Sun, S. Liu, L. Qiu, Z. Fang, and Y. Zheng, "A broadband resonant noise matching technique for piezoelectric ultrasound transducers," *IEEE Sensors J.*, vol. 20, no. 8, pp. 4290–4299, Apr. 2020.

[19] G. Turin, "An introduction to matched filters," *IRE Trans. Inf. Theory*, vol. 6, no. 3, pp. 311–329, Jun. 1960.

[20] D. Borio, "A statistical theory for GNSS signal acquisition," Ph.D. dissertation, Dept. Elect. Eng., Polytech. Univ. Turin., Turin, Italy, 2008.

[21] M. C. Chen, A. P. Perez, S.-R. Kothapalli, P. Cathelin, A. Cathelin, S. S. Gambhir, and B. Murmann, "A pixel pitch-matched ultrasound receiver for 3-D photoacoustic imaging with integrated delta-sigma beamformer in 28-nm UTBB FD-SOI," *IEEE J. Solid-State Circuits*, vol. 52, no. 11, pp. 2843–2856, Nov. 2017.

[22] J. A. Fredenburg and M. P. Flynn, "A 90-MS/s 11-MHz-bandwidth 62-dB SNDR noise-shaping SAR ADC," *IEEE J. Solid-State Circuits*, vol. 47, no. 12, pp. 2898–2904, Dec. 2012.

[23] Y.-S. Shu, L.-T. Kuo, and T.-Y. Lo, "An oversampling SAR ADC with DAC mismatch error shaping achieving 105 dB SFDR and 101 dB SNDR over 1 kHz BW in 55 nm CMOS," *IEEE J. Solid-State Circuits*, vol. 51, no. 12, pp. 2928–2940, Dec. 2016.

[24] J. Chang, A. A. Abidi, and C. R. Viswanathan, "Flicker noise in CMOS transistors from subthreshold to strong inversion at various temperatures," *IEEE Trans. Electron Devices*, vol. 41, no. 11, pp. 1965–1971, Nov. 1994.

[25] M. van Heijningen, J. Compiet, P. Wambacq, S. Donnay, M. G. E. Engels, and I. Bolsens, "Analysis and experimental verification of digital substrate noise generation for epi-type substrates," in *IEEE J. Solid-State Circuits*, vol. 35, no. 7, pp. 1002–1008, Jul. 2000.

[26] S. Kousai, M. Hamada, R. Ito, and T. Itakura, "A 19.7 MHz, fifth-order active-RC Chebyshev LPF for draft IEEE802.11n with automatic quality-factor tuning scheme," *IEEE J. Solid-State Circuits*, vol. 42, no. 11, pp. 2326–2337, Nov. 2007.

[27] J.-M. Stevenson and E. Sanchez-Sinencio, "An accurate quality factor tuning scheme for IF and high-Q continuous-time filters," *IEEE J. Solid-State Circuits*, vol. 33, no. 12, pp. 1970–1978, Dec. 1998.

[28] S. Chatterjee, Y. Tsividis, and P. Kinget, "0.5-V analog circuit techniques and their application in OTA and filter design," *IEEE J. Solid-State Circuits*, vol. 40, no. 12, pp. 2373–2387, Dec. 2005.

[29] J. Mahattanakul and J. Chutichatuporn, "Design procedure for two-stage CMOS opamp with flexible noise-power balancing scheme," *IEEE Trans. Circuits Syst. I, Reg. Papers*, vol. 52, no. 8, pp. 1508–1514, Aug. 2005.

[30] Y. Wang, M. Koen, and D. Ma, "Low-noise CMOS TGC amplifier with adaptive gain control for ultrasound imaging receivers," *IEEE Trans. Circuits Syst. II, Exp. Briefs*, vol. 58, no. 1, pp. 26–30, Jan. 2011.

[31] H.-C. Tsai, C.-L. Lo, C.-Y. Ho, and Y.-H. Lin, "A 64-fJ/conv.-step continuous-time sigma delta modulator in 40-nm CMOS using asynchronous SAR quantizer and digital delta sigma truncator," *IEEE J. Solid-State Circuits*, vol. 48, no. 11, pp. 2637–2648, Nov. 2013.

[32] R. T. Baird and T. S. Fiez, "Linearity enhancement of multibit $\Delta\Sigma$ A/D and D/A converters using data weighted averaging," *IEEE Trans. Circuits Syst. II, Analog Digit. Signal Process.*, vol. 42, no. 12, pp. 753–762, Dec. 1995.

[33] C. Chen, Z. Chen, D. Bera, E. Noothout, Z.-Y. Chang, M. Tan, H. J. Vos, J. G. Bosch, M. D. Verweij, N. de Jong, and M. A. P. Pertijs, "A 0.91 mW/element pitch-matched front-end ASIC with integrated sub-array beamforming ADC for miniature 3D ultrasound probes," in *IEEE Int. Solid-State Circuits Conf. (ISSCC) Dig. Tech. Papers*, Feb. 2018, pp. 186–188.

[34] E. Kang, M. Tan, J.-S. An, Z.-Y. Chang, P. Vince, N. Senegond, T. Mateo, C. Meynier, and M. Pertijs, "A 2pA/√Hz transimpedance amplifier for miniature ultrasound probes with 36 dB continuous-time gain compensation," in *IEEE Int. Solid-State Circuits Conf. (ISSCC) Dig. Tech. Papers*, Feb. 2020, pp. 354–356.

[35] G. Jung, M. W. Rashid, T. M. Carpenter, C. Tekes, D. M. J. Cowell, S. Freear, F. L. Degertekin, and M. Ghovanloo, "Single-chip reduced-wire active catheter system with programmable transmit beamforming and receive time-division multiplexing for intracardiac echocardiography," in *IEEE Int. Solid-State Circuits Conf. (ISSCC) Dig. Tech. Papers*, Feb. 2018, pp. 188–190.

ZESHENG ZHENG was born in Fujian, China. He received the B.Eng. degree from Nanyang Technological University, Singapore, in 2017, where he is currently pursuing the Ph.D. degree with the School of Electrical and Electronic Engineering. His research interests include photoacoustic/thermoacoustic for non-destructive sensing and imaging.

CHUANSHI YANG (Member, IEEE) received the B.Sc. degree from Shandong University, China, in 2012, the M.Eng. degree from Southeast University, China, in 2015, and the Ph.D. degree from Nanyang Technological University, Singapore, in 2020. His current research interests include high-resolution low power ADC and interface circuits for ultrasound sensors.

KAI TANG received the B.S. degree in information and computing science, the M.S. degree in software engineering (IC design), and the Ph.D. degree in circuits and system from Southeast University, China, in 2005, 2008 and 2014, respectively. From 2013 to 2014, he was a Ph.D. International Exchange Student at the School of Electrical and Electronic Engineering, Nanyang Technological University (NTU), Singapore, where he is currently working as a Research Fellow with the VIRTUS, IC Design Center of Excellence. His current research interests include analog circuits, data converter, transceivers for CMOS FMCW/pulsed chirp Radar, Lidar, and phased array.

ZHONGYUAN FANG (Member, IEEE) received the B.Sc. degree (Hons.) in microelectronics from Fudan University, in 2016. He is currently pursuing the Ph.D. degree with Full Scholarship with the Electrical and Electronic Engineering Department, Nanyang Technological University, Singapore. From 2014 to 2016, he was an Undergraduate Research Assistant at the State Key Laboratory of ASIC and System, Shanghai. Since 2016, he has been with the Virtus IC Design Center of Excellence, Singapore. His work has published in several leading conferences and journals. His research interests include analog/mixedsignal and low-power integrated circuit design, energy-efficient algorithms for physiological signal extraction, AI-enabled IC design, and RF/wireless communication circuits and systems design and testing for biomedical applications. He received the Excellent Student Scholarship from Fudan University, in 2016. He was a recipient of the Fudan Science and Technology Innovation Award.

XIAOYAN TANG received the B.S. degree in electronic engineer from Xian Jiaotong University, Xi'an, China, and the M.S. degree in electronic engineering from Nanyang Technological University, Singapore. She worked as a digital system engineer in industry for years. Since 2014, she has been working with the School of EEE, Nanyang Technological University for digital system design and implementation of digital communication and neural networks.

YUANJIN ZHENG (Senior Member, IEEE) received the B.Eng. and M.Eng. degrees from Xi'an Jiaotong University, Xi'an, China, in 1993 and 1996, respectively, and the Ph.D. degree from Nanyang Technological University, Singapore, in 2001. He was at the National Key Laboratory of Optical Communication Technology, University of Electronic Science and Technology of China, Chengdu, China, from 1996 to 1998. In 2001, he joined the Institute of Microelectronics (IME), Agency for Science, Technology and Research, Singapore, where he was a Principal Investigator and the Group Leader. In 2009, he joined Nanyang Technological University, where he is currently the Center Director of VIRTUS IC Design Center of Excellence and the Program Director for VALENS Bio Instrumentation, Devices and Signal Processing. With IME, he led and developed various projects like CMOS RF transceivers, baseband system-on-chip (SoC) for wireless systems, ultrawideband, and low-power biomedical ICs. He has authored or coauthored over 500 international journals and conference papers, several book chapters, and holds 30 patents filed/granted. His current research interests include gigahertz radio frequency integrated circuit and SoC design, biosensors and imaging, and surface acoustic wave/bulk acoustic wave/microelectromechanical sensors. He has been organizing over 15 conferences as TPC and session chairs and has delivered over 25 invited talks at international conferences. He was an Associate Editor of IEEE TRANSACTIONS ON BIOMEDICAL CIRCUIT AND SYSTEMS. He currently serves as an Associate Editor for *IEEE Journal of Electromagnetics, RF and Microwave in Medicine and Biology* (J-ERM).

• • •